Superconductor
Science and
Technology

PAPER

Role of microstructure on flux expulsion of superconducting radio frequency cavities

To cite this article: B D Khanal *et al* 2025 *Supercond. Sci. Technol.* **38** 015015

IOP Publishing
Superconductor Science and Technology
Supercond. Sci. Technol. **38** (2025) 015015 (18pp)
https://doi.org/10.1088/1361-6668/ad9ad7

Role of microstructure on flux expulsion of superconducting radio frequency cavities

B D Khanal[1], **S Balachandran**[2], **S Chetri**[3], **M Barron**[4], **R Mullinix**[3], **A Williams**[3], **P Xu**[5], **A Ingrole**[6], **P J Lee**[3], **G Ciovati**[1,2] **and P Dhakal**[1,2,*]

[1] Department of Physics, Old Dominion University, Norfolk, VA 23529, United States of America
[2] Thomas Jefferson National Accelerator Facility, Newport News, VA 23606, United States of America
[3] Applied Superconductivity Center, NHMFL-FSU, Tallahassee, FL 32310, United States of America
[4] Indiana University-Purdue University of Indianapolis, Indianapolis, IN 46202, United States of America
[5] Brookhaven National Laboratory, Upton, NY 11973, United States of America
[6] Magnet Science and Technology, NHMFL-FSU, Tallahassee, FL 32309, United States of America

E-mail: dhakal@jlab.org

Received 16 September 2024, revised 11 November 2024
Accepted for publication 5 December 2024
Published 16 December 2024

Abstract

The trapped residual magnetic flux during the cool-down due to the incomplete Meissner state is a significant source of radio frequency losses in superconducting radio frequency cavities. Here, we clearly correlate the niobium microstructure in elliptical cavity geometry and flux expulsion behavior. In particular, a traditionally fabricated Nb cavity half-cell from an annealed poly-crystalline Nb sheet after an 800 °C heat treatment leads to a bi-modal microstructure that ties in with flux trapping and inefficient flux expulsion. This non-uniform microstructure is related to varying strain profiles along the cavity shape. A novel approach to prevent this non-uniform microstructure is presented by fabricating a 1.3 GHz single cell Nb cavity with a cold-worked sheet and subsequent heat treatment leading to better flux expulsion after 800 °C/3 h. Microstructural evolution by electron backscattered diffraction-orientation imaging microscopy on cavity cutouts, and flux pinning behavior by dc-magnetization on coupon samples confirms a reduction in flux pinning centers with increased heat treatment temperature. The heat treatment temperature-dependent mechanical properties and thermal conductivity are reported. The significant impact of cold work in this study demonstrates clear evidence for the importance of the microstructure required for high-performance superconducting cavities with reduced losses caused by magnetic flux trapping.

Keywords: microstructures, flux expulsion, SRF cavity, superconductor

1. Introduction

Superconducting radio frequency (SRF) cavities are the building blocks of modern particle accelerators for fundamental scientific discoveries, security and defense, energy and medical isotope production, materials research, and quantum information systems [1, 2]. In recent years, material research has focused on increasing the Q_0 in the medium accelerating gradient range ($\sim$20 MV m^{-1}) by lowering the BCS resistance of SRF cavity with ‘dirty’ surface layers by impurity diffusion through the Nb surface (titanium, nitrogen, oxygen) [3–10]. The success of this fundamental R&D discovery is reflected in the adoption of nitrogen treatment in the LCLS-II protocol for producing hundreds of multi-cell cavities commissioned for the LCLS-II cryomodules [11]. The quest for the highest Q_0 and cryogenic efficiency has focused on minimizing surface resistance by surface engineering.

---

[*] Author to whom any correspondence should be addressed.

Traditionally, the starting raw material for forming SRF Nb cavities has been annealed Nb sheet with fine grain sizes ~50 μm (ASTM 4–8). However, cavities have also been fabricated from Nb sheets with medium grain sizes of few mm and large grain with centimeter-scale grain sizes. Fine-grain sheets have better formability characteristics than larger-grain Nb sheets and are preferred for large production batches. Large grain sheets have performance and cost benefits provided repeatable process design can be achieved [12, 13]. Once fabricated, the cavities receive recipe-based surface treatments to create a dirty superconducting layer on the interior surface of the cavity, which improves the quality factor provided that no magnetic flux is trapped. Experimental evidence and theoretical studies indicate that the increase in surface resistance due to trapped magnetic flux due to insufficient flux expulsion during the cavity cool-down through the transition temperature severely degrades the performance [14–19]. Early studies on poorly flux-expelled cavities shows that increasing the heat treatment temperature beyond the traditional 800 °C/3 h can improve flux expulsion [20, 21]. With the increase in heat treatment temperature, the grain size is increased while the density of pinning centers (grain boundaries and dislocations) decrease. Coupon studies of SRF-grade Nb suggest that flux trapping and expulsion are related to microstructural dimensions: (a) large grains are better at expelling flux, and (b) regions containing fine grains embedded in large grains preferentially trap magnetic flux in fine grain regions [22]. Material defects in bulk Nb, such as dislocations and segregation of impurities, provide favorable sites for magnetic flux pinning and contribute to additional losses when exposed to the rf field [23–25]. The Nb surface also plays an important role in pinning and rf losses due to vortices [26]. Generally, impurity-diffused cavities are more vulnerable to vortex-induced losses due to the presence of impurities on the surface of the cavity [16, 20, 27, 28]. Heat treatment, which leads to recrystallization and grain growth, is the main mechanism for reducing the bulk material defects in an SRF Nb cavity. Choosing a suitable cavity heat treatment to maximize the flux expulsion has been complex for cavities: higher heat treatment temperatures result in reduced Nb strength at room temperature [29], and different heat treatment temperatures were found for cavities made of Nb sheets from different vendors and batches [20, 30]. Recently we reported that fabricating cavities with a cold-worked Nb sheet leads to improved flux expulsion performance after 800 °C in cavities, irrespective of the vendor [31].

In this manuscript, we show that 800 °C/3 h can be a sufficient heat treatment condition for full flux expulsion from an SRF cavity fabricated from a non-annealed sheet provided by a vendor whereas previously a higher heat treatment temperature was needed for cavity fabricated from a conventional sheet from the same vendor. This work provides a pathway for low defect SRF Nb cavities starting from a cold-worked Nb sheet and further heat treating to 800 °C/3 h to obtain better flux expulsion in an SRF cavity. The lower heat treatment temperature is preferable to maintain the strength of the Nb cavities at room temperature. We reconfirm that the flux expulsion behavior is a bulk microstructure phenomenon, and spatial distribution of uniform microstructure rather than large average grain sizes is an important factor for flux expulsion. This first result directly correlates bulk cavity microstructure with flux expulsion performance through half-cell coupon studies. To better understand the cold-work Nb, physical and mechanical properties were measured to provide an envelope for the applicability of the new starting state of Nb that can be used to fabricate SRF cavity with better flux expulsion. It is to be noted that the duration of heat treatment is limited to 3 hours at all temperatures throughout this study.

2. Cavity fabrications and sample preparation

2.1. Cavity fabrications

A fine grain Nb sheet of thickness ~3 mm was purchased according to the material specification for LCLS-II from the vendor, Tokyo Denkai, Japan. In addition, a special order was made from the vendor to provide sheets in the cold-worked state without the final heat treatment performed by the vendor, and no further post-processing. The vendor did not provide any material specifications. This new sheet does not meet the current SRF Nb specifications. The details about the high purity niobium sheet production steps are presented in [32]. The residual resistivity ratio and the impurity concentrations provided by the vendor are shown in table 1. Electron backscattered diffraction–orientation images (EBSD-OI) acquired for the two sets of Nb sheets are compared in figure 1. For the production of the half-cells, the Nb sheets were machined to discs with outer diameters of 266.7 mm and inner diameters of 47 mm, the same dimensions used for the center cell of 9-cell TESLA-shaped SRF cavity [33]. The deep drawing dies available in-house were made from fully anodized aluminum alloy. The half-cells were formed using a male and female die set. The shape deviations of the half-cells were inspected with a 3D scanner and ~85% of the points were within ±0.2 mm from the ideal shape for SRF-grade and ~71% for coldworked Nb as shown in figure 2. A large deviation is seen at the iris region for the cold-worked sheet, which may be corrected by refining the profile of the die for deep drawing. The local shape variation in the iris and equator regions corresponds to 296 ±41 μm, and 212 ± 27 μm, which are in the range of the measurements made with the 3D scanner.

The fabrication of the cavities followed the standard practice of trimming, machining of the iris and equators of the half-cells, and finally electron beam welding of the beam tube (made from low-purity niobium). The regions to be welded were chemically etched by buffered chemical polishing (BCP) to remove ~20 μm of material after machining. During the equator weld, a failure in the electron beam welding process created holes that were repaired with Nb plugs with an e-beam melt using the Nb material from the available sheet.

After fabrication, the cavities were electropolished (EP) in a horizontal, rotating setup, using a mixture of electronic grade HF:H_2SO_4 = 1:9 at a constant voltage of ~14 V, a temperature of 15–20 °C and a speed of 1 rpm. A total bulk depth of ~150 μm at cavity equator was removed by EP. The first cycle of the heat treatment of the cavity was done at 800 °C for 3 h

Table 1. Purity and status of the niobium used for the fabrication of the two single cell cavities used in this study.

Cavity name	Nb specification, supplier	Bulk RRR	Ta (wt. ppm)	H (wt. ppm)	C (wt. ppm)	O (wt. ppm)	N (wt. ppm)
TCA-01	SRF grade, Tokyo Denkai	393	11	<5	<1	<1	<1
TCNA-01	Cold work, Tokyo Denkai	212[a]	–	–	–	–	–

[a] RRR is estimated from the thermal conductivity measurements.

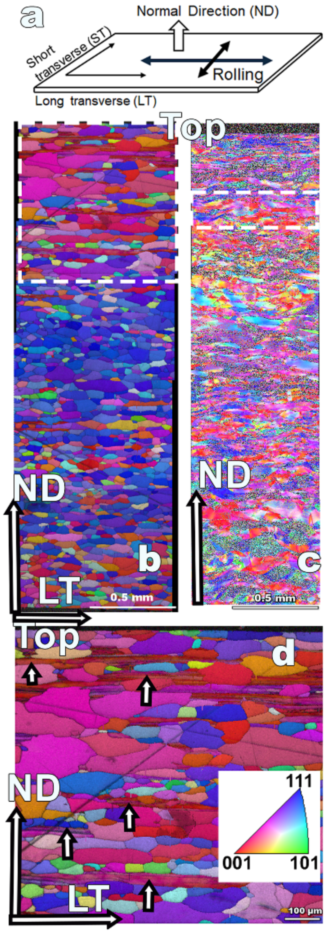

Figure 1. Initial microstructure of the cross rolled Nb sheets for cavity fabrication (a) schematic of rolling direction (b) and (c) EBSD of SRF-grade and as rolled niobium along ND and (d) near-surface details of SRF grade sheet.

in a UHV furnace. The cavity was further EP'ed before the rf test. Successive heat treatments of 900 °C and 1000 °C for 3 h followed by 25 μm EP were applied before each rf test.

2.2. Coupons sample preparation

Several cylindrical samples of diameter 1 mm and 3 mm in length were machined from the cold-work sheet to quantify flux pinning by dc magnetization measurements. One additional half-cell was deep-drawn and machined to get strips from the equator to the iris of the cavity. The machined surface of the strips was chemically etched by BCP. The strips and cylinder samples were processed along with the cavities to replicate the processing technique applied to the Nb cavities. Cross-sectional EBSD-OI was performed to evaluate the metallurgical state of the niobium. Additionally, bar samples of 70 $\times$ 3 $\times$ 3 mm^3 were machined and processed with high-temperature heat treatment to measure the thermal conductivity. Small sample coupons $\sim$10 $\times$ 6 $\times$ 3 mm^3 were machined and polished to measure the Vickers Hardness (HV) and cross-sectional microstructure measurements.

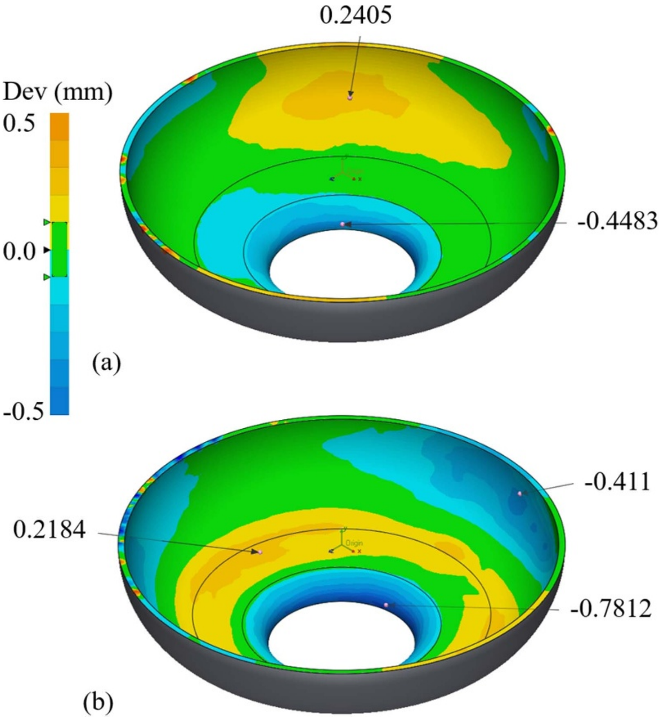

Figure 2. 3D scan of half-cells and comparison with design for (a) SRF grade and (b) cold-worked Nb. The region in green corresponds to a deviation within ±0.1 mm.

3. Experimental setup

3.1. Cavity test

Three single-axis cryogenic flux-gate magnetometers (FGM) (Mag-F, Bartington) were mounted on the cavity surface parallel to the cavity axis ~120° apart to measure the residual magnetic flux density at the cavity outer surface during the cool-down process. The magnetic field uniformity within the cavity enclosure is ~ ± 1 mG. Six calibrated temperature sensors (Cernox, Lakeshore) were mounted on the cavity: two at the top iris, ~180° apart, two at the bottom iris, ~180° apart, and two at the equator, close to the FGM. The distance between the temperature sensors at the top and bottom iris was ~20 cm.

The measurement process was in two parts: firstly, several cooldown and warm-up cycles were performed above 10 K to explore the flux expulsion ratio while changing the temperature gradient along the cavity axis. The second part of the measurement procedure is as follows: (i) the magnetic field was initially set below 2 mG using the field compensation coil surrounding the vertical Dewar. (ii) The standard cavity cool-down process was applied, resulting in < 0.1 K temperature difference between the top and bottom iris. The temperature and magnetic field were recorded until the Dewar was full with liquid He and a uniform temperature of 4.3 K was achieved. This step assumes that all the applied magnetic fields are trapped in the SRF cavity walls. (iii) $Q_0(T)$ at low rf field (peak surface rf magnetic field $B_p \sim 20$ mT) from 4.3–1.6 K was measured using the standard phase-lock technique. (iv) Q_0 vs B_p was measured at 2.0 K. (v) The cavity was warmed up above T_c and the residual magnetic field in the Dewar is set to certain values (~20 and ~40 mG). Steps (ii) to (iv) were repeated for two different magnetic field values.

3.2. dc magnetization

Isothermal magnetic hysteresis loops were obtained by applying the external dc magnetic field along the cylinder's axis using a 5 T Quantum Design magnetic property measurement system. The applied magnetic field ($B_a = \mu_0 H_a$) was then corrected to include the demagnetization and replaced with the effective magnetic field ($B_{\text{eff}} = \mu_0 H_{\text{eff}}$) using the relation, $H_{\text{eff}} = H_a - 4\pi NM$ (in CGS units) where N is the demagnetization factor which, for a cylindrical sample, is given by [34]:

$$N = 1 - \frac{1}{1 + q\frac{a}{b}}. \tag{1}$$

Here,

$$q = \frac{4}{3\pi} + \frac{2}{3\pi}\tanh\left[1.27\frac{b}{a}\ln\left(1 + \frac{a}{b}\right)\right] \tag{2}$$

where $b/a = 3$ is the length-to-diameter ratio of the cylindrical sample. The pinning force was determined by using the relation $F_{\text{p}} = B_{\text{eff}} \times J_{\text{c}}$, where J_{c} is the critical current density obtained from the magnetic hysteresis loop using the Bean model and given by $J_{\text{c}} = 15\Delta M/r$, where ΔM is the difference in magnetization for B_{eff} during increasing and decreasing field in the hysteresis loop, and r is the radius of the cylinder.

3.3. Thermal conductivity

Experimental thermal conductivity measurements were performed using an in-house setup and procedures developed for the measurement of thermal conductivity of Nb in the temperature range of 1.8–6 K as described in [35]. The apparatus is immersed in liquid helium, and lower temperatures are obtained by pumping the liquid helium to sub-atmospheric pressure. A heater was installed at one end of the sample and the other end was exposed to superfluid helium. In steady state, the thermal conductivity, κ of the specimen as a function of temperature (T) is given by

$$\kappa = \frac{Pd}{A\Delta T} \tag{3}$$

where P is the power supplied to the resistive heater, d is the distance between two temperature sensors installed on the specimen, $\Delta T = T_1 - T_2$ is the temperature difference between two temperature sensors and A is the cross-sectional area of the specimen.

3.4. Microstructural analysis

The cross-sectional microstructure of the Nb samples was analyzed using a scanning electron microscope. Samples were prepared for metallographic analysis by hot-mounting using a conductive bakelite compound, Konductomet®. The samples were sequentially ground down to obtain flat surfaces with 320, 400, 600, 800, and 1200-grit SiC pads. Diamond polishing with sequential grit sizes of 5 μm, 3 μm, and 1 μm was used for subsequent polishing followed by vibratory polishing using a Vibromet II® using a 50 nm colloidal silica solution (Mastermet®)with a pH of 11.5. An intermediate light chemical polishing with a BCP 1:1:2, hydrofluoric acid (HF): nitric acid (HNO_3): phosphoric acid (H_3PO_4) was performed; the final step involved re-polishing in the Vibromet® to achieve damage-free cross-sections. Orientation imaging microscopy (OIM) was performed with an EDAX Velocity® camera capable of greater than 2000 indexed points per second and angular precision below 0.1° in a LaB_6 filament, Tescan Vega 3 microscope. Data analysis was performed using EDAX-TSL-OIM software version 8.5.1002.

3.5. Tensile testing

Dog-bone-shaped tensile as per ASTM- 10^{-8} standard was machined from the cold work sheet along the rolling direction (RD), 45° to RD, and perpendicular to RD to obtain in-plane mechanical deformation characteristics of the Nb sheet in this study. Annealing of the cut tensile samples after BCP was performed by heat treating at 800 °C, 900 °C, and 1000 °C in a UHV furnace used for SRF cavity heat treatments. Mechanical behavior, including stress and in-plane strain behavior, was recorded for the Nb sheet to evaluate formability. Only the modulus and strength of the sheets will be presented here. Four tensile samples with and without heat treatment were tested using a MTS Criterion station, with a load cell with 5 kN capacity, under displacement control at a strain rate of 5×10^{-5} s^{-1}. A Class B, 25 mm initial gauge length tensile extensometer with a strain range of 20 % was used to record the longitudinal strain data. A digital image correlation system measured the deformation along the length and thickness. The tensile tests were stopped at criteria when the load dropped by 10%

of the maximum load reached. This also corresponds to a well-developed neck in the specimen, after which instabilities dominate the local deformation. The yield strength (YS) ($\sigma_{y,0.002}$), referred to as σ_y or YS, and ultimate tensile strength (UTS) are reported based on the engineering stress values based on the initial cross-sectional area. Since the cold work Nb sheet was from the same heat and batch number as the SRF Nb specified sheet that was used to make the traditional cavity, we do not report the properties of the traditional sheet here. We are of the opinion that the heat treatments performed on the cold worksheet are sufficient to capture the mechanical properties of the traditional SRF Nb sheet from the vendor.

3.6. Vicker hardness and recrystallization

Samples of nominal dimensions $\sim 6 \times 4 \times 3$ mm^3 were cut from the non-annealed sheet for the heat treatment study. Heat treatments were performed at 300 °C–1000 °C. The ramp rate used for the study was 5 °C min^{-1}. The heat treatments between 300 °C–700 °C were performed by sealing the samples in an evacuated quartz tube with high-purity Ar (Airgas UHP-400). The 800 °C–1000 °C samples were heat treated in a vacuum furnace used in cavity heat treatments. After heat treatments, Vickers microhardness (HV) tests were conducted on the polished cross-section samples using a Starrett Micro Vickers/Knoop Hardness Tester. The hardness results reported here were conducted using an indenter load of 300 g, and a dwell time of 15 s, per ASTM 10-384–05a [36].

3.7. Half-cell cutout

During the cavity fabrication, two additional half-cells were deep drawn, one of each from the cold work and SRF grade sheets. The half-cells were cut in strips from the equator to the iris to evaluate the cross-sectional microstructure. The strips were chemically etched $\sim 50\,\mu$m followed by the UHV heat treatment at 800, 900, and 1000 °C. The strips were cut into sections that were hot-mounted using a conductive bakelite compound and polished using the sample procedure described above. Electron microscopy and Vickers hardness were measured along the cross-section of the samples.

4. Cavity test results

4.1. Cool-down and flux expulsion

The ratio of the residual dc magnetic field measured after (B_{sc}) and before (B_n) the superconducting transition qualitatively explains the effectiveness of the flux expulsion during the transition. A value of $B_{sc}/B_n = 1$ represents complete trapping of the magnetic field during cool-down, whereas a flux expulsion ratio of ~ 1.7 at the equator would result from the ideal superconducting state. Experimentally, B_{sc}/B_n depends on the Nb material and on the temperature gradient along the cavity axis during the cool-down. Values of B_{sc}/B_n close to the theoretical estimate could be achieved with a high-temperature gradient ($\mathrm{d}T/\mathrm{d}s > 0.3$ K·cm^{-1}). A representative plot of the residual magnetic field at the FGM's locations measured during one cool-down cycle for cavity TCA-01 is shown in figure 3. The average value of B_{sc}/B_n for the three FGMs at the equator was 1.55 ± 0.03. The temperature difference between the top and bottom iris when the equator of the cavity reached the superconducting transition temperature $\sim$9.25 K is 3.28 K.

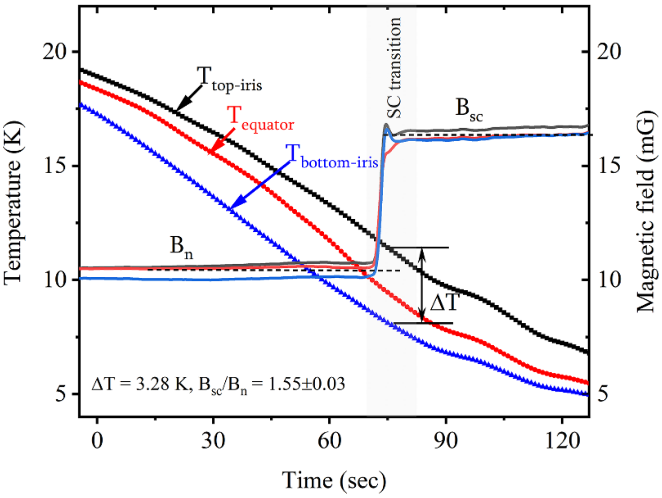

Figure 3. Temperature and magnetic field during the transition from normal to superconducting state measured during a cool-down cycle of cavity TCA-01.

Figure 4 shows the flux expulsion ratio B_{sc}/B_n for both cavities concerning the temperature gradient after each heat treatment. The flux expulsion for the cavity made from cold work Nb showed a better expulsion for the cavity heat treatment at 800 °C compared to SRF grade Nb. The flux expulsion ratio is similar for both cavities when heat treated with an additional 900 °C. However, the cavity made from cold-worked sheets showed better flux expulsion after an additional 1000 °C heat treatment. The dependence of flux expulsion on temperature difference showed different characteristics depending on the heat treatment temperature.

4.2. RF measurements

The average rf surface resistance was obtained from the measurement of $Q_0(T)$ at low rf field ($B_p \sim 20$ mT) for different applied dc magnetic fields, B_n, before each cool-down. The data were fitted with the following equation:

$$R_s(T) = R_{\mathrm{BCS}}(T, \omega, l, \Delta) + R_{\mathrm{res}}, \tag{4}$$

where the BCS surface resistance R_{BCS} was computed numerically from the Mattis–Bardeen (M–B) theory [37] using Halbritter's code [38]. The mean free path, l, and the ratio $\Delta/k_B T_c$ were regarded as fit parameters, where Δ is the energy gap at $T = 0$ K, and k_B is the Boltzmann constant. We used a coherence length of $\xi_0 = 39$ nm and the London penetration depth, $\lambda_0 = 32$ nm for Nb in the clean limit, $\xi_0 \ll l$ at $T = 0$.

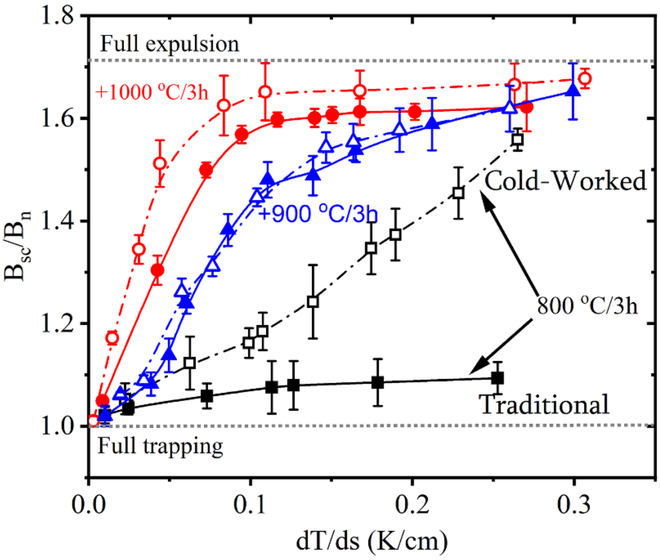

Figure 4. Average flux expulsion ratio at the equator of SRF cavity as a function of the temperature gradient (iris-to-iris) after each cavity treatments for TCA-01 made from SRF grade traditional Nb (solid symbols) and TCNA-01 made from cold worked Nb (open symbols). The lines are guide to the eye.

The residual resistance R_{res} was extracted for different trapped magnetic fields. The T_c of the cavity was measured during the cavity warm-up.

Figure 5 shows the residual resistance as a function of the trapped dc magnetic field before the cavity transitions from the normal to superconducting state, B_n, in full flux trapping condition, $B_{sc}/B_n{\sim}1$, where $\triangle T < 0.1$ K.

The residual resistance due to trapped flux can be written as:

$$R_{\text{res}}(B_n) = R_0 + \eta_t S B_n, \tag{5}$$

where R_0, plotted in figure 6, accounts for the contributions to R_{res} other than trapped flux. This could be non-superconducting nano-precipitates, sub-oxide layers at the surface, or a broadening of the density of states [39]. η_t, is the flux trapping efficiency and S the sensitivity to magnetic flux. For $\triangle T < 0.1$ K, it is assumed $\eta_t \sim 1$, and S gives the flux trapping sensitivity, allowing the extraction of S from the slope in figure 5.

The $Q_0(B_p)$ measured at 2.0 K after cool-down with dT/ds > 0.2 K·cm^{-1} and $B_n{\sim}0$ mG for each cavity and treatment is shown in figure 7. All RF tests were limited by quench, and the low quench field may be attributed to the fabrication issue we encountered during cavity welding.

In order to obtain information about the mean free path near the surface, we measured the resonant frequency and quality factor while warming up the cavities from ~ 5 K to higher than the transition temperature (>9.3 K) using a vector network analyzer, from which $R_s(T)$ and the change in resonant frequency was extracted. A representative plot of surface resistance and change in frequency during warm-up is shown in figure 8. The frequency shift can be translated into a change in penetration depth according to

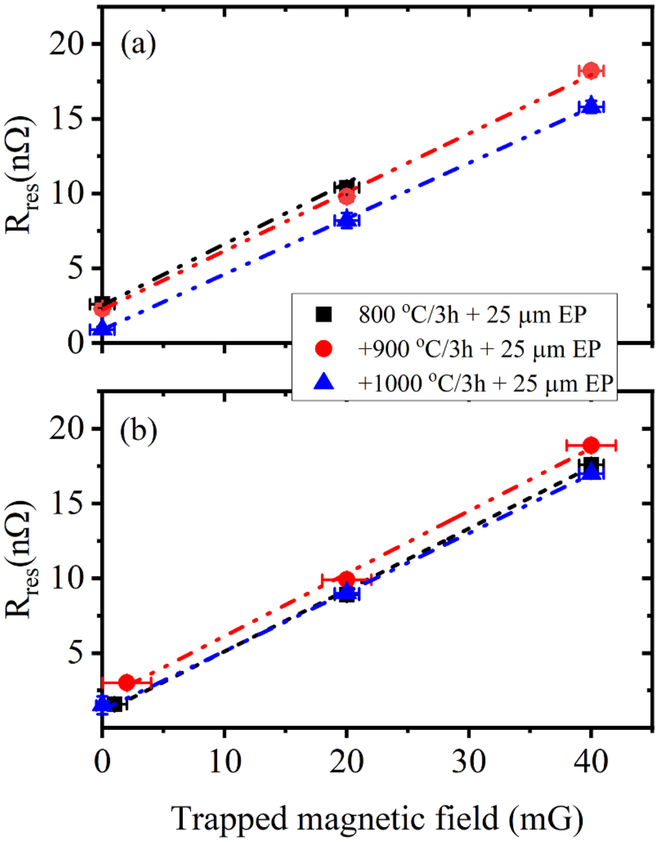

Figure 5. The residual resistance as a function of trapped field after each treatment stage for cavity (a) TCA-01 (traditional sheet) and (b) TCNA-01.

$$\Delta\lambda = \frac{G}{\pi\mu_0 f^2}\Delta f \tag{6}$$

with G being the geometric factor of the cavity, f as the resonant frequency. Using the Casimir-Gorter relation [40], we can obtained λ_0, which is the penetration depth at 0 K as:

$$\Delta\lambda = \lambda(T) - \lambda_0 = \frac{\lambda_0}{\sqrt{\left(1-(T/T_c)^4\right)}} - \lambda_0. \tag{7}$$

In the Pippard limit [41], λ_0 is directly related to the mean free path of the quasi-particles as:

$$\lambda_0 = \lambda_L\sqrt{1+\frac{\pi\xi_0}{2l}}. \tag{8}$$

The value of the London penetration depth λ_L and coherence length of the Cooper pairs ξ_0 taken are the same that were used in the $R_s(T)$ fit. Figure 9 shows the $\Delta\lambda_L$ vs reduced temperature, y. The data in the superconducting state were fitted using the numerical solution of M–B theory. Table 2 summarizes all the results of the rf measurements.

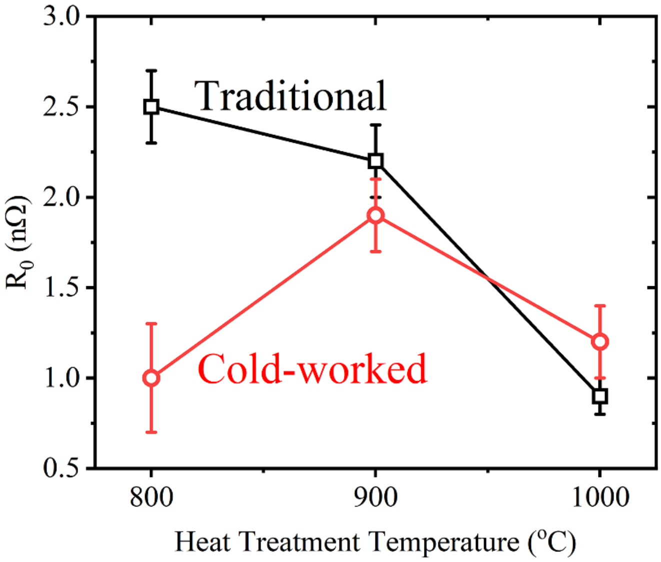

Figure 6. The intrinsic residual resistance due to non-superconducting nano-precipitates, sub-oxide layers at the surface, broadening of the density of states [39] for cavity TCA-01 and TCNA-01 after each heat treatment followed by ∼25 μm EP.

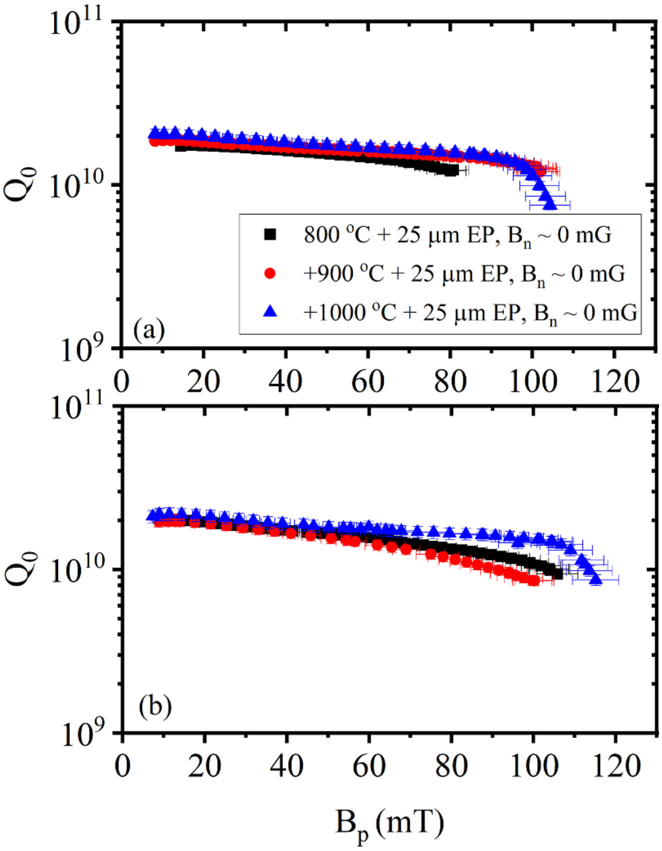

Figure 7. $Q_0(B_p)$ measured at 2.0 K after cool-down with $dT/ds > 0.2\,\mathrm{K{\cdot}cm^{-1}}$ and $B_n \sim 0$ mG for cavity (a) TCA-01 and (b) TCNA-01. All rf tests were limited by quench.

5. Analysis of deep-drawn half-cell

5.1. Hardness profile

The Nb sheet deformed into a half-cell shape retains characteristics of the deformation process. Figure 10 shows the hardness as a function of location along the half-cell cross-section, from the equator to the iris, for the conventional SRF grade Nb. In the deep-drawn state shown by the curve in blue, the highest hardness of $HV_{0.3}\sim$ 100 occurs at the iris region, closely followed by the hardness within the first 20 mm of the equator region where the hardness is $HV_{0.3}\sim$ 90. There is a

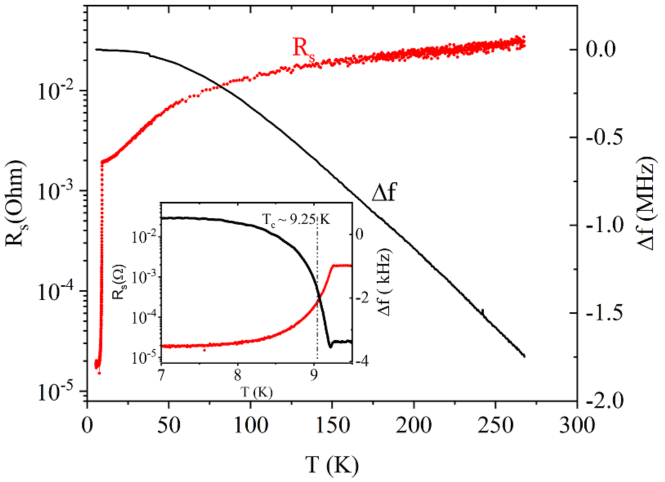

Figure 8. The surface resistance and change in resonant frequency as a function of temperature during cavity warm up. The inset shows the superconducting to normal conducting transition at $T_c\sim$ 9.25 K.

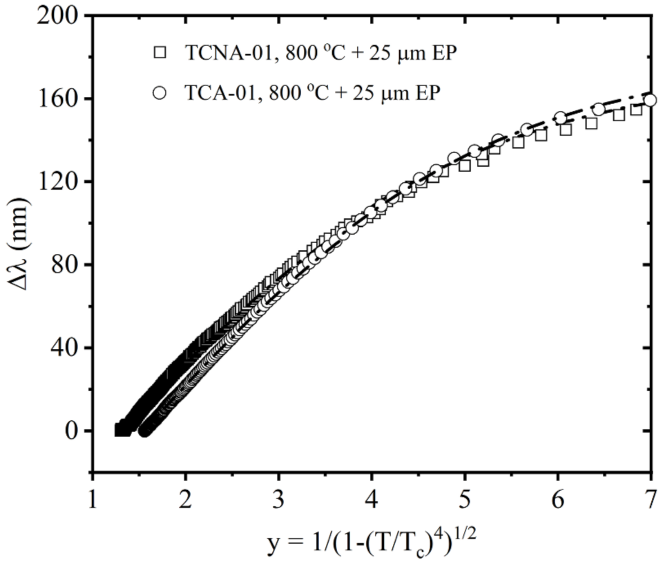

Figure 9. Change of penetration depth as a function of the reduced temperature parameter $y=1/\sqrt{1-(T/T_c)^4}$ measured on cavity TCNA-01 and TCA-01 after 800 °C heat treatment followed by ~25 μm EP. The dash-dotted lines are fit with M–B theory.

Table 2. The flux trapping sensitivity S obtained from fits of $R_{\mathrm{res}}(B_n)$ for different treatments and weighted average values of $\Delta/k_B T_c$ obtained from fits of $R_s(T)$ between 1.6 – 4.3 K for each cavity. The mean free path l was obtained from the fit of $\Delta\lambda_L$ (T) and T_c was measured during the cavity warm up.

Cavity name	Treatment	S (nΩ/mG)	$\Delta/k_B T_c$	l(7.5 – 9.25 K) (nm)	T_c (K)
TCA-01	800 °C + 25 μm EP	0.44 ± 0.01	1.78 ± 0.02	315 ±2	9.25 ± 0.05
	+900 °C + 25 μm EP	0.43 ± 0.01	1.80 ± 0.02	296 ±2	9.24 ± 0.02
	+1000 °C + 25 μm EP	0.40 ± 0.01	1.80 ± 0.02	386 ±9	9.25 ± 0.03
TCNA-01	800 °C + 25 μm EP	0.45 ± 0.01	1.79 ± 0.02	375 ±6	9.26 ± 0.03
	+900 °C + 25 μm EP	0.43 ± 0.01	1.81 ± 0.02	389 ±6	9.25 ± 0.01
	+1000 °C + 25 μm EP	0.40 ± 0.01	1.80 ± 0.02	475 ±4	9.23 ± 0.03

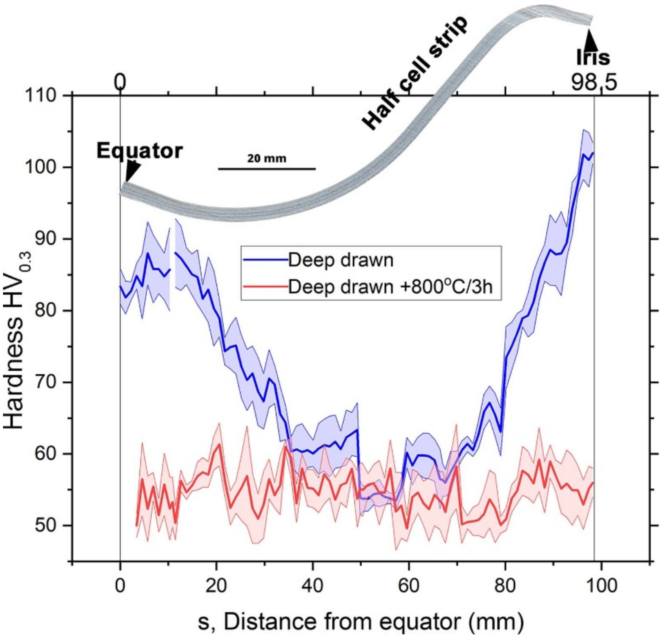

Figure 10. Hardness profile from the equator to iris region from a half-cell fabricated with a traditional SRF Nb sheet with an initial microstructure as shown in figure 1 in as deformed state and after 800 °C heat treatment.

gradual drop in hardness from the high hardness regions at the iris and equator towards the center of the half-cell, which is at $HV_{0.3}\sim 50$. The variation in the hardness as a function of half-cell location after an 800 °C/3 h heat treatment shows that the hardness is reduced to a uniformly low level of $HV_{0.3}\sim 50$–60 across the entire length from iris to equator, thus the higher the initial hardness the greater the drop in hardness. At the very center of the half-cell the hardness is the same before and after heat treatment.

5.2. Development of microstructure after half-cell deformation and 800 °C

Sheets with different initial processing histories (annealed and cold-worked) were drawn into half-cells to simulate the cavity fabrication operation and then annealed at 800 °C to reduce the effects of the deformation history and aid in the recovery of the crystalline damage. The analysis focused on the hardness profiles developed for the traditional sheet in figure 10. Samples were carefully selected from three different locations: Region a, around the iris region; Region b, 40–50 mm along the profile from the equator region; and Region c, corresponding to 20–30 mm from the equator region. The inverse pole figures (IPF) maps are plotted to show the crystal orientation plane parallel to surface plane normal direction (ND). Thus, in a SRF cavity, the ND direction represents the functional SRF surface. The IPF maps have dark regions (shown in black) indicating a low confidence index ($CI < 0.1$), implying that the orientations could not be resolved, either due to step size-related resolution of the deformation structure or the sample conditions (i.e surface cleanliness or charging artifacts).

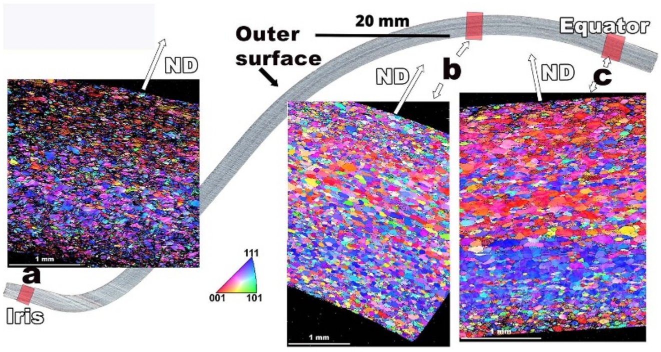

Figure 11. IPF maps of selected regions in the ND to the half-cell surface normal showing the variation in deformation in the different areas of the cavity half-cell, (a) close to the iris, which is heavily deformed, (b) and (c) are around the equator regions with lesser deformation. Region c has slightly higher deformation than region b. After half-cell fabrication, the texture gradient is present between the top and bottom surfaces.

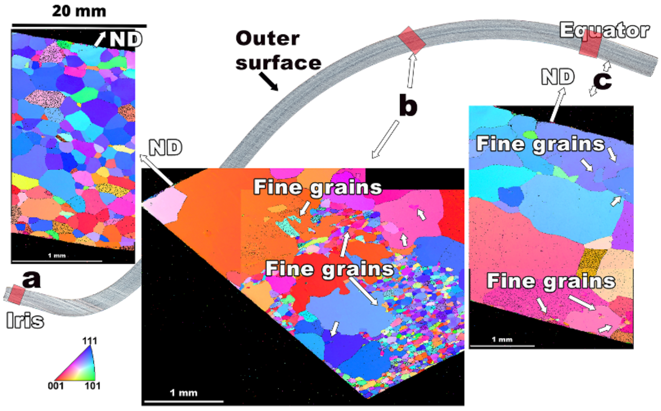

Figure 12. IPF maps of selected regions in the ND to the half-cell surface normal showing the variations in recrystallization and grain growth in different areas of the cavity half-cell, (a) close to the iris, has fine-grain equiaxed microstructure, and (b) and (c) contain large abnormal grains and finer grains that appear to be trapped inside these large grains.

5.2.1. Traditional Nb sheet formed into half-cell.

Figure 11 presents the (IPF) map of a cross-section of a traditional sheet deep-drawn to a half-cell. The significant deformation in the iris region is evident in figure 11(a), as observed by the in-grain orientation gradients and the change in the aspect ratio of the microstructure (flattened). In contrast, regions b and c exhibit less deformation, where the microstructure of the parent sheet, along with the initial grains, is apparent. Region c, closest to the equator, shows slip traces in the grains, visible in the high-magnification image in figure 12, indicative of light deformation. In all the above IPFs, there are texture gradients across the through-thickness cross-sections.

After an 800 °C annealing heat treatment, the microstructure changes from the deformed parent structure indicated in figure 11 to a recrystallized and grain growth structure in figure 12. The initially heavily deformed iris region a, has an equiaxed microstructure with an average grain size of 100 μm.

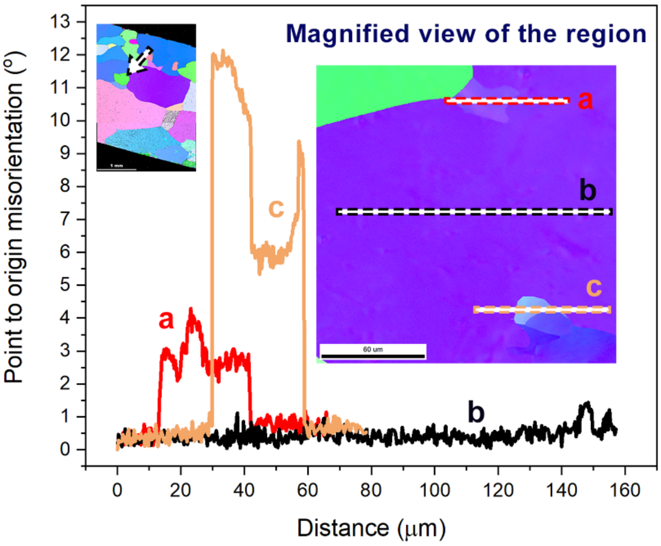

Figure 13. Line scans measuring the misorientation inside the abnormally large grain close to the equator in region c, show the finer details of the abnormal large grains. These regions have local misorientations as low as 2° (a) and as high as 12° (c). The line scan in (b) indicates an expected in-grain line misorientation profile; the variations along the length are the noise floor in the measurement. Note: The IPF map is the same as that of region c in figure 12 but plotted in a different color scheme to identify the boundaries visually.

Whereas, the lightly deformed regions, b and c, corresponding to figures 12(b) and (c) show an abnormal grain growth phenomenon with large grains of 100's of μm and embedded variations in crystal orientations resembling refined grains of tens of micrometers with distinct boundaries. Abnormal grain growth refers to a few large grains that grow abnormally large compared to other surrounding grains in a polycrystalline matrix [42]. A magnified image of a section of the abnormally grown areas indicates a finer structure, as shown in figure 13. There are boundaries inside and along the boundaries of the abnormally grain-grown regions. The point to origin line misorientation in figure 13 indicates the boundaries encountered are misoriented by $\leqslant 15^\circ$ as shown by the line scans in (a) and (c). The line scan in (b) shows the misorientation within the grain crossing no boundaries and can be interpreted as the noise expected with the dataset.

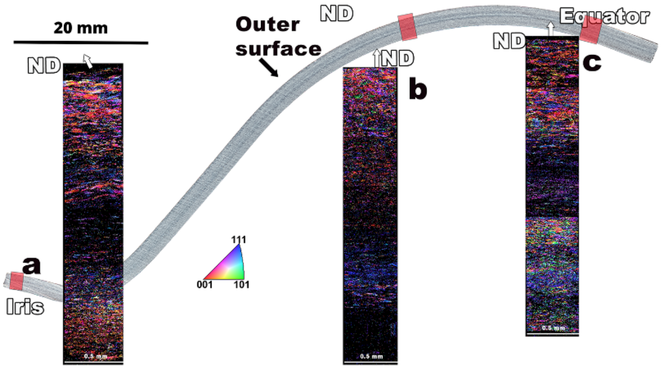

Figure 14. IPF maps of selected regions in the ND to the half-cell surface normal from the half-cell fabricated with an initially cold-worked sheet showing un-indexed regions in the microstructure corresponding to heavy deformation-related ambiguity determining the crystal orientation with a relatively large step size scans of 1 μm. The observed charging artifacts in the signal are the result of the sample being mounted in non-conducting epoxy.

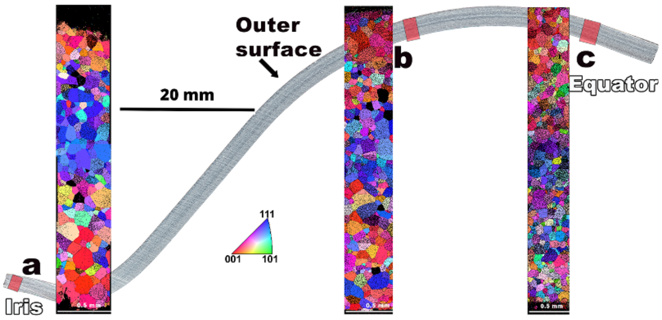

Figure 15. IPF maps of selected regions in the ND to the half-cell surface normal from the half-cell fabricated with an initially cold-worked sheet after 800 °C heat treatments showing an equiaxed uniform microstructure in the different regions of the half-cell. The observed charging artifacts in the signal result from the sample being mounted in non-conducting epoxy.

5.2.2. Non-traditional sheet formed into half-cell. The half-cell formed from an initial cold-worked sheet must have been better indexed in the different regions analyzed for this study, as shown in figure 14. The detailed deformed microstructure would need higher-resolution imaging of the areas, which is beyond the scope of this study. The purpose is to compare the traditional versus the newer 'non-traditional' approach, leading to a higher overall deformation throughout the half-cell. After an 800 °C heat treatment, the non-traditional-sheet formed half-cell has a more equiaxed microstructure compared to the traditional-sheet formed half-cell, as seen in figure 15. Unfortunately, due to variations in the sample preparation, charging issues were encountered with the non-traditional samples, limiting the direct quantitative comparisons between the traditional and non-traditional sheets regarding micro-texture and local misorientations.

However, with the data generated during this study, we have compared the quantitative variations in the grain size after the 800 °C heat treatments between the traditional and non-traditional approaches in figure 16. The grain size in the iris region a, which was more deformed in the traditional route, results in an average grain size of 100 μm with a full-width half maximum bandwidth of 75–300 μm, after heat treatment, whereas the equator and intermediate regions which underwent lower deformation led to abnormal grain growth with a multi-modal grain size distribution centered around 300, 500, and 1000 μm. In the case of the non-traditional half-cell, we find that the grain size distributions for each region are more uniform and overlap, being centered around 100 μm.

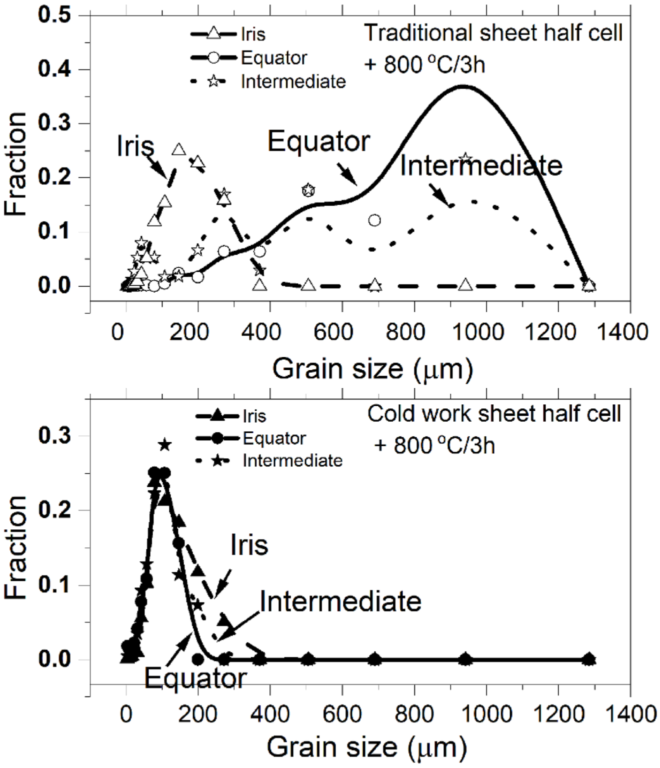

Figure 16. Grain size distributions for the different regions of the traditional sheet formed half-cell indicating multi-modal distributions in the equator and intermediate regions, whereas the non-traditional sheet formed half-cell has similar single-mode distributions for each region, with an average grain size of 100 μm.

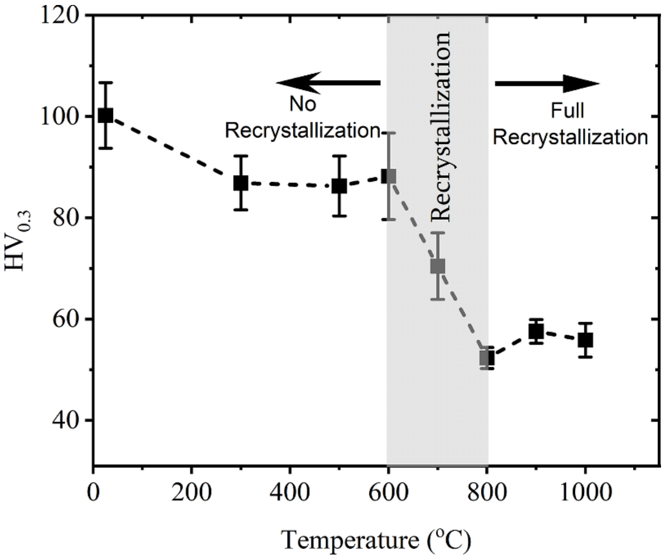

Figure 17. Vickers hardness measured on cross-sections of cold-worked Nb as a function of heat treatment temperature. The line is a guide to the eye.

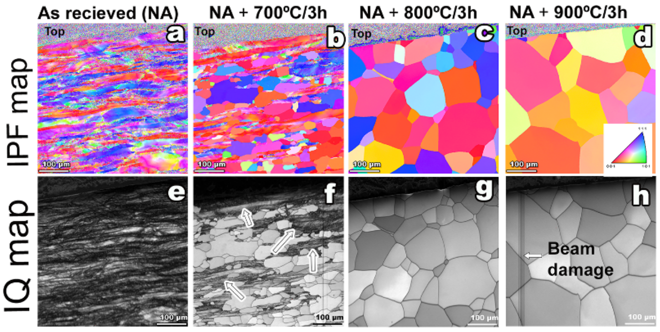

Figure 18. Inverse pole figures (IPF), for the sheet cross-sections as a function of heat treatment in the (a) non-traditional initial cold-worked sheet, (b) after 700 °C, (c) after 800 °C, and (d) after 900 °C, and (e), (f), (g) and (h) are the corresponding image quality (IQ) maps respectively.

6. Coupon sample characterization

6.1. Recrystallization of as received cold-worked Nb sheet

The cold-worked Nb sheet from the vendor to form the half-cell was received before the conventional final recrystallization anneal. We observed the recrystallization behavior of the as-received material by plotting the measured hardness ($HV_{0.3}$) as a function of annealing temperature in the range of 300 °C–1000 °C, at a constant soaking time of 3 h. The recrystallization curve in figure 17 shows that the hardness decreases as a function of temperature. There is a 10% drop in the hardness from the initial cold-work hardness after a 300 °C anneal, a 30% drop in initial hardness for the 700 °C sample, and a nearly 50% drop in hardness after the 800 °C heat treatment which is maintained after a subsequent 900 °C–1000 °C heat treatment.

The corresponding microstructure of the samples after different heat treatment conditions is shown in the IPFs and the image quality (IQ) maps in figure 18. The cold-worked Nb microstructure in figure 18(a) and (e) is one of the elongated grains running parallel to the sheet surface, and the high deformation levels appear dark in the IQ map. After 700 °C, new recrystallized grains are visible in figures 18(b), (f) and appear lighter in the IQ map, whereas the deformed microstructure appears darker. After 800 °C, there are no deformed regions present in the microstructure images in figures 18(c), (g), and grains are equiaxed with larger grains of the order of 100 μm, and some finer grains in the range of 20–30 μm. After 900 °C, grain growth of the equiaxed grain sizes with more significant fractions of grains in the 100 μm range are observed in figures 18(d) and (f). To quantify the variations in grain size as a function of heat treatment temperature, we plotted the grain size distribution in figure 19; the average grain size increases from 50 μm after 700 °C to 125 μm after 900 °C, with a bi-modal distribution appearing at 800 °C. An interesting observation from this dataset is that the conventional specification for the average grain size at 50 μm corresponds to a mixture of worked and recrystallized microstructure and not a fully recrystallized one.

6.2. Thermal Conductivity

The temperature dependence of thermal conductivity for different samples under study is shown in figure 20. The

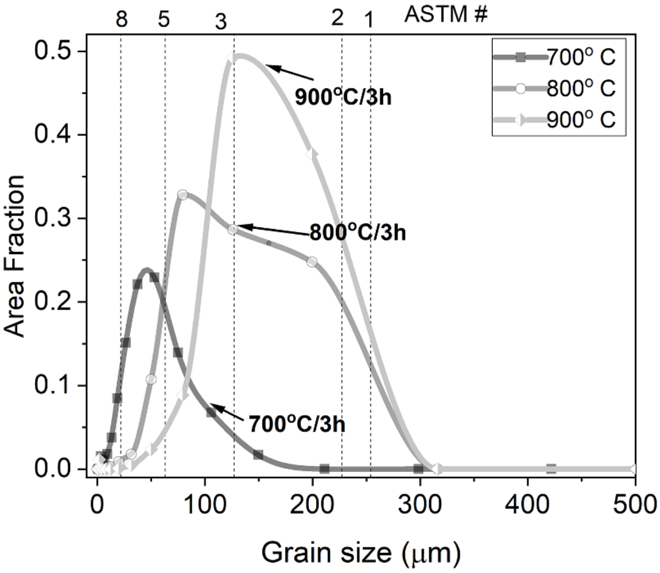

Figure 19. Grain size distribution as a function of heat treatment temperature.

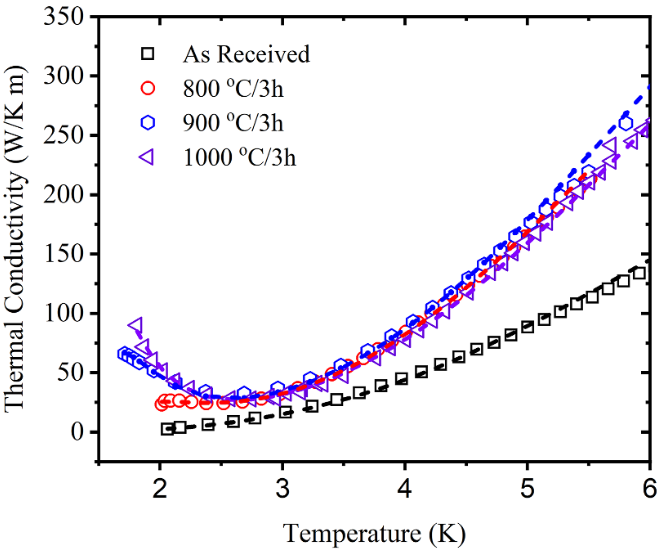

Figure 20. The temperature dependence of thermal conductivity for as-received and heat-treated samples. The dashed lines fit to thermal conductivity.

thermal conductivity of the as-received, cold-worked sample is 2.3 W K^{-1}·m at 4.2 K, corresponding to a RRR value of 212. As a result of heat treatment, the thermal conductivity at 2.0 K increased to 23.2, 45.3 and 51.6 W K^{-1}·m after the high-temperature heat treatment, corresponding to RRR values of ∼ 400. The thermal conductivity data were fitted using the model developed by Xu [43] incorporating randomly distributed dislocation structures. The model predicts the dislocation density by relating the effect of dispersion due to dislocations. Based on the fit, the predicted dislocation density in the as-received material is 4.7×10^{13} and decreases to 1.14×10^{12} after 800 °C heat treatment. A previous study on single crystal Nb showed that this change in dislocation density corresponds to the ∼5% uniaxial strain present in as-received sheet [44]. Additionally, the phonon mean free path was estimated to be ∼1.75 μm for as received samples increasing to ∼50 μm after 800 °C heat treatment. The phonon means free path is qualitatively in agreement with the grain size since, at low-temperature, phonons are scattered by grain boundaries.

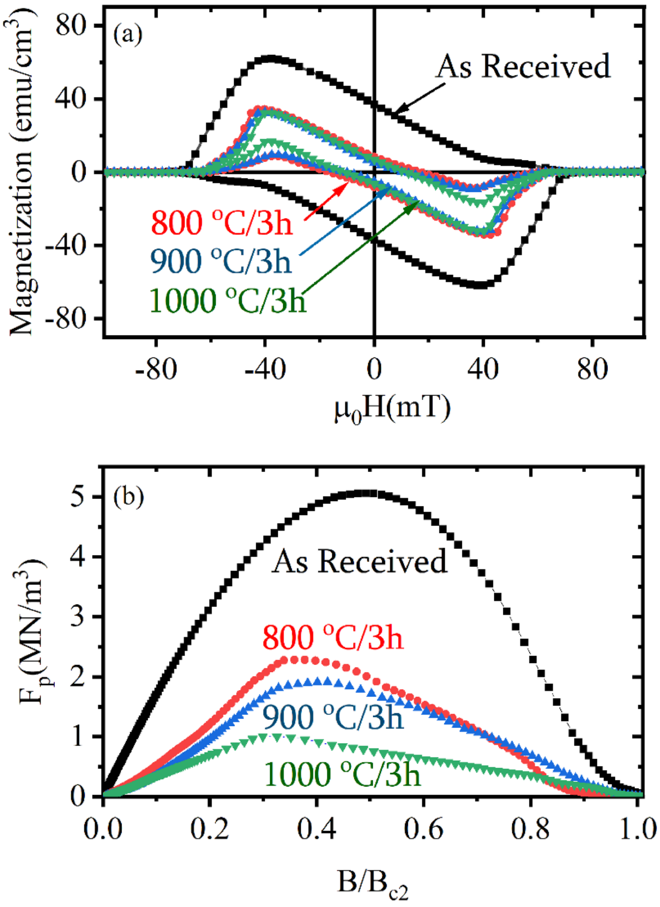

Figure 21. The isothermal dc magnetic hysteresis of the cold-worked Nb samples in zero field cooled state measured at 8.0 K. (b) Pinning force as a function of reduced magnetic field at 8.0 K.

6.3. *dc Magnetization and Pinning*

The isothermal dc magnetic hysteresis of the samples in zero-field cooled state measured at 8.0 K is shown in figure 21(a). The area under the hysteresis loop decreases as we increase the heat treatment temperature, demonstrating the overall reduction in bulk pinning centers from the niobium sample. The pinning force was calculated at 8.0 K and plotted as a function of the reduced magnetic field (B/B_{c2}) as shown in figure 21(b). The maximum pinning force (F_p) of the cold-worked Nb is ∼ 5 MN m^{-3} and it decreases to ∼2.2 MN m^{-3} after the 800 °C heat treatment. A further decrease in maximum pinning force

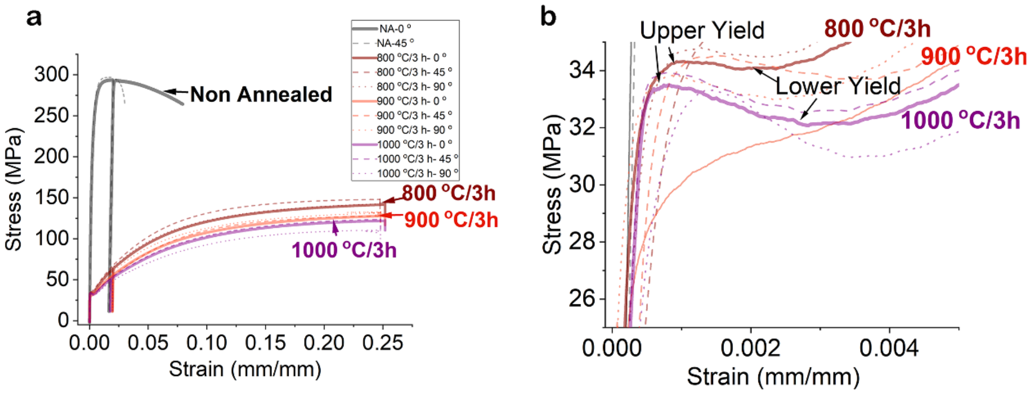

Figure 22. (a) Tensile test curves from the non-traditional cavity sheet after different heat treatments up to 25% engineering strain. Notice the significant drop in strength after an 800 °C heat treatment. (b) The initial part of the stress–strain curve indicates the phenomena of upper and lower yield point in the annealed material.

was observed when the samples were heat treated at higher temperature. The reduction in pinning force is expected due to the removal of pinning sites as a result of heat treatment [45]. Furthermore, there is no significant change in the pinning force behavior as seen from the location of the peak. The experimental data does not fit with any single pinning model [46], nevertheless the peak at higher reduced field corresponds to the core collective (volume, surface and point) $\delta\kappa$ pinning, where the size of the pinning or the spacing between them are within the penetration depth. The pinning force peak at $B/B_{c2}{\sim}0.5$ is mostly dominated by volume pinning, whereas the peak shift towards the lower values ~0.3–0.4 suggests that the dominating pinning mechanism is point pinning due to the segregation of normal conducting precipitates [46].

6.4. Mechanical properties

Figure 22 shows the in-plane tensile tests performed on the non-annealed (NA) samples and after heat treatments to evaluate deformation characteristics in 0°, 45°, and 90° to the RD. The main difference between the tensile properties of the NA and the heat-treated samples are the following: Material strength is higher in the NA condition versus the heat-treated condition- 800 °C. The uniform deformation is lower in the NA state versus the heat-treated samples. The uniform deformation is inferred from the beginning of the drop in stress due to sample necking in the engineering stress–strain curve. In the NA samples, the instability occurs at lower strain values of less than 5%. In contrast, instability in the heat-treated samples does not occur beyond a strain of 20% as evidenced by the flat-near plastic deformation of polycrystalline Nb. In the heat-treated samples, the initial deformation has an interesting yield behavior as shown in figure 22(b). Most heat-treated tensile test samples have an upper and lower yield point, irrespective of the orientation. To quantify the mechanical properties, stress–strain parameters, which include the elastic modulus (EM), YS at 0.2% strain, and the UTS, and the Vickers micro-hardness ($HV_{0.3}$) is reported in table 3. The modulus of the Nb sheet material varies between an average modulus of 73–87 GPa, with the lowest modulus occurring in the NA sheet material. The highest modulus of 89 GPa occurs after a 1000 °C heat treatment. No clear trends are observed between the orientation and in-plane strength values in the directions tested. However, minor variations are observed in the in-plane strength characteristics. The in-plane variation in the YS for the NA sheet is 4%, and UTS is 2%. In the samples after 800 °C, and 900 °C the variation in in-plane YS and UTS is less than 3%. In the 1000 °C sample the variation in the UTS is slightly higher ~7%. From the above data, we plot the variation in YS as a function of grain size (d), as shown by the classical Hall–Petch relationship [47], equation (9),

$$\sigma_y = \sigma_0 + \frac{k}{\sqrt{d}} \tag{9}$$

where, σ_0 is the material's intrinsic strength related to the critical resolved shear stress, k is the Hall–Petch coefficient, and d is the grain size. Figure 23, provides the relationship that fits the experimental data with, $\sigma_0 = 23.3$ MPa, and $k = 139$ MPa. $\mu\mathrm{m}^{1/2}$. The obtained YS values are within the 10% trend lines of the recent measurements on recrystallized SRF cross-rolled Nb sheets [48, 49]. Based on the Hall–Petch fit, we can estimate the yield of the material once the grain size is determined. For the cold-worked, as-received material, the average Y.S. is 258 MPa; from the Hall–Petch equation, we obtain an average grain size of 0.35 μm. However, the Hall–Petch model may not apply to the cold-worked sheets with no well-defined grain sizes.

7. Discussion

7.1. Impact of the initial sheet microstructure on cavity deformation and heat treatment

Figure 10 shows the spatial variation in hardness between ~50 in the mid-section and high hardness of 80–100 in regions close to the equator and iris regions, respectively. As the material deforms and yields, strain-hardening and microhardness are closely correlated. Since the deformation during

Table 3. Summary of mechanical properties of the cold-worked sheet in the as-received and heat-treated conditions.

Sample condition	Orientation (°)	EM (GPa)	YS (MPa)	UTS (MPa)	HV $_{0.3}$	YS : HV$_{0.3}$	UTS : HV$_{0.3}$
Non- annealed (NA)	0	73	268	294	100 ± 5	2.6	2.7
	45	73	258	298			
	90	73	249	304			
Average		73	258 ± 10	299 ± 5			
NA + 800 °C/3 h	0	82	34	144	50 ± 2	0.7	2.9
	45	72	35	149			
	90	82	34	145			
Average		79 ± 6	34 ± 1	146 ± 3			
NA + 900 °C/3 h	0	84	31	130	58 ± 2	0.6	2.2
	45	75	34	128			
	90	79	33	133			
Average		79 ± 5	33 ± 2	130 ± 3			
NA + 1000 °C/3 h	0	87	32	123	56 ± 1	0.6	2.1
	45	89	31	124			
	90	86	32	110			
Average		87 ± 2	32 ± 1	119 ± 8			

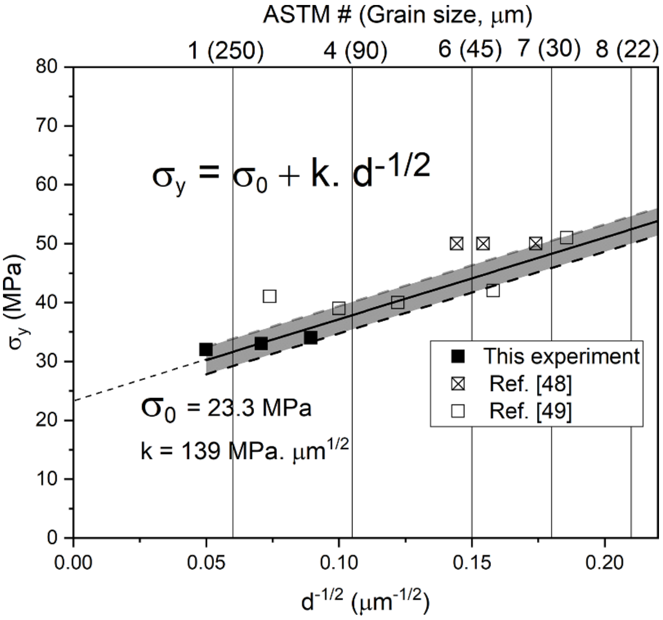

Figure 23. Hall–Petch plot of yield strength as a function of grain size is consistent with the expected linear trend and previous studies.

deep drawing varies along the cavity profile, the hardness also changes accordingly. For SRF Nb, the variation in the hardness provides a proxy for the total strain experienced by the material. The high-strain regions are close to the equator and iris. The hardness is lowered to a fully annealed material level after the 800 °C heat treatment. The result of the location-based hardness curve of the annealed sheet is a characteristic of the average macro strain expected in the cavity.

The results from this study demonstrate that cavities can be manufactured from sheets with retained cold work with no changes to the tooling, dies, or fabrication steps. Initially, cold-worked sheets maintain high levels of prior deformation in the half-cell regions from the equator to the iris and maintain higher dislocation densities that are not indexed with confidence (CI $\geqslant 0.1$) within the step size of the limit of micrometers as shown in figure 14. The cavity formed with a traditional annealed sheet consists of non-uniform cold work as the half-cell shape is formed, as shown by the IPFs in figure 11 between the iris and the equator. The complete cross-section microstructure also indicates that there may be non-uniform deformation within the sheet cross-section in the annealed starting material.

The strain profile along the cavity half-cell shape directly impacts the microstructural evolution after the 800 °C heat treatment. The main difference between the microstructural evolution during heat treatment is: in the traditional half-cell, a bi-modal microstructure exists throughout the half-cell structure except the heavily deformed iris region. In the moderately and lightly strained regions abnormal grain growth in the order of 100's of μm and embedded finer grains in the order of 30–50 μm in the cross-section as shown in figure 12(b), and low angle boundary structures in figure 12(c) occur, whereas, equiaxed microstructure in figure 12(a) occurs in the iris region. The low-angle grain boundaries suggest that the heat treatment temperature cannot fully sweep the stable or pinned low-angle boundaries formed during the recovery stages. This leads to an incomplete recrystallized grain [50]. The abnormal grain growth at 800 °C in very high purity Nb in regions of low strain may be related to a lack of nucleation points due to low strains and impurities leading to a few grains, possibly due to favorable orientations growing rapidly over others. In high-strain regions, a more uniform distribution of nucleation sites for new grains could lead to a more uniform grain size.

In the half-cell fabricated with cold-worked sheets, the level of deformation is high prior to the deep drawing. After heat treatment, a more uniform microstructure is observed as shown in figure 15, with the grain size curves from different regions overlapping around a mean value of $\sim$100 μm as shown in figure 16. The tails of the curves in figure 16 are slightly different among the other regions, indicating that even with the available initial cold work in this study combined with the half-cell deformation, the grain growth characteristics may still be somewhat different between the regions. The iris region c, has an overall sharper distribution compared to the region a, and region b. In terms of the strain path (hardness) for the half-cell deformation the strain in region a $>$ region c $>$ region b. These results prove that a critical amount of cold work is necessary to homogenize the grain size in cavity cross-sectional microstructures after 800 °C heat treatment. Otherwise, the cavity deformation, being spatially non-uniform, leads to a difference in microstructure, leading to regions of bi-modal large-fine grain structures within the sheet cross-section. The amount of critical cold work that is needed is unknown, but the vendor provided these sheets before any heat treatment step at the upstream processing step.

7.2. Impact of microstructure on flux expulsion

Figure 4 showed that the cavity fabricated from a cold-worked Nb sheet has improved flux expulsion characteristics after 800 °C compared to a cavity made from a traditional Nb sheet. The variation in flux expulsion behavior has been previously correlated to average grain size [21], implying that the larger the grain size the higher the flux expulsion. Here, we show that the average grain size in the traditional sheet after 800 °C heat treatment is location dependent and non-uniform, i.e. finer grains embedded in large grains as shown in figures 12 and 13. The average grain size is $\sim$150 μm at the iris and as high as 1 mm at the equator, as shown in figure 16. In the case of the cold-worked sheet cavity after 800 °C, the average grain size is $\sim$100 μm. However, after the 800 °C the flux expulsion performance is superior in the cavity fabricated with cold-worked sheet versus the traditional sheet. It is possible to achieve the full flux expulsion limit on cavities fabricated with cold work Nb after 800 °C heat treatment if one can maintain the temperature gradient between the cavity irises above 0.25 K cm^{-1}, which is not the case with cavities made from conventional SRF grade Nb. As shown in table 2, the flux trapping sensitivity does not change between the different starting sheets that have undergone similar surface treatments, consistent with the literature [26]. Fundamentally, our results show that the flux expulsion directly correlates to the non-uniformity of grain size rather than the average grain size. Previously, we have observed that a non-uniform, bi-modal grain size distribution leads to flux trapping and poor flux expulsion in fine grain regions [22]. These cavity results and the cavity cut-out microstructure strengthen the hypothesis that bi-modal, non-uniform fine-large grain structures possibly caused by inadequate recrystallization tend to show poorer flux expulsion. The shape of the flux expulsion curve is different depending on the temperature, irrespective of the initial sheet condition. For the 800 °C case, the flux expulsion ratio increases approximately linearly with the temperature gradient, whereas for the 900 °C and 1000 °C has a different behavior, showing a rapid expulsion of flux as the temperature gradient is increased. We interpret these results as related to the underlying microstructure and subtle variations between the surface and bulk grains. The interior surface of Nb cavity is highly susceptible to damage, and this damaged layer could influence the flux expulsion performance [24]. Based on recent results by Thune and co-workers [51–53], surface regions within the first few microns of the SRF niobium may recrystallize differently from the bulk, as suggested by the decreased surface recrystallized fractions after 800 °C and 900 °C heat treatments. Whereas the bulk recrystallizes 100% after 800 °C, which is also confirmed from the coupon study experiments of the hardness-based recrystallization curve in figure 17. The grain size distribution in figure 16 suggests a finer grain peak below 100 μm. The OIM in figure 18(c), suggests fine grains in the regions approximately within 10 μm from the surface. Other researchers have also observed surface abnormality in grain growth [21, 54], and this is the first interpretation directly linking to flux expulsion. We do not understand the exact nature of why these refined grains are present but speculate that dislocations may be blocked by surface barriers such as oxides [55], carbides [55–57], or other contaminants from the heat treatment furnace. It is well known that 800 °C dissolves the Nb pentoxide effectively [58]. The variations between the 800 °C and higher temperatures may be related to the inability of the dislocations that are getting annealed to go past the oxide barrier at low temperatures, leading to a surface zone of non-recrystallized or fine grain size layer. Gaining more statistics from the surface layers and comparing them with bulk microstructure as a function of temperature and chemistry can unequivocally answer this question. We can also infer from this result that decreasing the grain boundary density with heat treatment reduces the overall number of pinning sites, changing the shape of the flux expulsion curve. The pinning force curves in figure 21 show that as the heat treatment temperature increases, the pinning force drops, and there is a slight shift in the pinning force curve to the left. An open question remains whether variations in the DC pinning force curves indicate subtle changes in the pinning mechanism or whether surface effects dominate them.

7.3. Summary of coupon studies and relevance to SRF Nb cavities

Coupon studies provide a test bed to evaluate fundamental microstructural-physical property correlations relevant to SRF cavities. The coupon studies presented here provide quantitative microstructure data that could correlate with the cavity performance which is affected by flux expulsion or pinning, thermal conductivity, and early flux penetration. The mechanical property data could also provide engineering design guidelines that may help with pressure vessel code designs.

In this paper, following the recrystallization steps of an initial vendor-supplied non-annealed sheet, we find grain size dependence on recrystallization, mechanical strength, thermal conductivity (hence RRR), and pinning force curves. From our results here, figures 18 and 16, specification of finer grain size of 50 μm or lesser leads to an initial material that is not completely recrystallized. The impact of this incomplete initial recrystallization after deformation leads to low-strained regions in the cavities having dislocation structures solely due to the initial sheet condition rather than cavity deformation. As shown in figure 13, these remnant dislocation structures or lightly deformed regions can lead to bi-modal microstructure due to abnormal grain growth and retain dislocation structures that could decrease the Nb's ability to expel magnetic flux.

The thermal conductivity measurements indicate clear differences between non-annealed and recrystallized Nb, especially at 2 K, where the phonon modes are critical for heat transfer. However, at 4.2 K, there are no significant changes in the heat transfer characteristics. The RRR as inferred from the non-annealed sheet after 1000 °C varies between 200 to 400 depending on the initial sheet condition. Assuming that the sheet chemistry (mainly determined by the number of electron beam melting steps) does not change, we find that the variation in thermal conductivity and hence the RRR is a function of microstructure. The results here indicate that with increases in boundary density either due to a cold-worked state or low heat treatment temperature, the RRR can vary significantly. This can be expected in the range of 200–400 in a cavity after deformation and heat treatment. The dc-magnetization and pinning force curves in figure 21 also suggest the variation possible in the strength of the pinning force locally. The mechanical properties in table 3, and figures 22 and 17 indicate the variation in strength as a function of grain size and heat treatment, which needs consideration, especially in designing for pressure vessel codes [29, 59]. From the Hall–Petch equation for Nb determined here, large surface grains of the order of millimeters like those in Figure 12 lead to local soft spots due to a decrease in YS. This decrease in local YS could lead to cavity shape changes during handling, directly impacting cavity tuning. These large/bi-modal grains have also been observed before during the SNS project (2000's) and LCLS-II (present) [21, 60]. In general, keeping the impurity content constant, the strength is a function of grain size for a given purity of SRF Nb. An essential consideration for SRF is surface roughness, and quantifying the average surface roughness in the uniform deformation region of the various samples shows the influence of the initial microstructure on the roughness. Different areas of cavities may need different amounts of removal to achieve the same smoothness. Implications of this varying roughness based on grain size that may exist apriori in Nb sheets may lead to regions of different roughness when optimization based on dirty layer removal is prioritized [61]. The open question is the impact of surface roughness on the enhancement of flux penetration, and recent work suggests that topographic defects substantially suppress the superheating field and, hence, in the reduction of an achievable accelerating gradient in SRF cavities [62]. From the half-cell deformation studies, the non-annealed sheet develops a uniform microstructure in different regions of the cavity, and the impact of the varying physical, electromagnetic, and thermal properties is likely to be minimized.

7.4. Adoption of cold-worked sheet into mainstream cavity fabrication

Cold-worked sheets benefit the flux expulsion behavior, particularly at low heat treatment temperatures, by aiding better recrystallization. The strength of SRF Nb depends primarily on the grain size or grain boundary density. The lower the grain size, the higher the GB density and the better the strength as indicated in figure 16, and table 3. Choosing lower heat treatment temperatures and obtaining superior performance, i.e. high Q_0, by lowering the residual resistance is possible in SRF cavities from any vendor if a cold-worked sheet is chosen over a traditional sheet. However, adopting this strategy for cavity manufacture will require exploring the formability ranges of cold-worked Nb sheets. A uniaxial test shows a low uniform deformation of 5% at 45° in-plane to the RD and 10% along the RD, suggesting low in-plane deformability. Nb is highly formable and can be simulated by parametrized models to predict bi-axial deformation. The extent of deformability depends on the strain rate, and servo controls available [63]. The lack of uniform deformation could be an issue with cavity shapes and needs exploration of the formability diagram [64]. Annealed sheets show uniform work hardening and good formability beyond 25% in-plane after heat treatments of the initial cold-worked sheet.

8. Summary

We have successfully fabricated and tested 1.3 GHz TESLA-shaped cavities made with non-traditional sheets with retained cold-work, and lower uniform in-plane deformation. Half-cell experiments, using the standard deformation path for such cavities, reveal continuous hardness variations from the equator to the iris, corresponding to the variation in the deformation path during deep drawing. These deformation path variations lead to microstructural variations after 800 °C heat treatment. Specifically, there exist bi-modal grain size distributions, with regions containing fine (50–100 μm) and large (greater than 100 μm) grains. The flux expulsion and trapping sensitivity variability was measured on cavities made from cold worked (non-annealed) and traditional SRF grade Nb. We find better flux expulsion after heat treatment in cavities made from cold-worked Nb compared to the cavity made from traditional annealed SRF grade Nb [65]. The direct correlation between the importance of uniform recrystallization and flux expulsion is established. No variations were observed in terms of $Q_0(E_{\mathrm{acc}})$ and flux trapping sensitivity as long as the final surface preparation remains the same. Adopting a new sheet strategy would need further exploration, including developing new specifications and additional optimization focused on maximizing the microstructural benefits of using non-annealed sheets. Several single-cell cavities were fabricated using different levels of cold-work Nb sheet, and results will be made available in future publications.

Data availability statement

The data that support the findings of this study are available upon reasonable request from the authors.

Acknowledgments

We acknowledge Jefferson Lab technical staff members for the cavity fabrication, processing, cryogenic, and rf support. The work done at Florida State University is supported by the U S Department of Energy, Office of Science, Office of High Energy Physics under Awards No. DE-SC 0009960 (FSU) and the State of Florida. Additional support for the National High Magnetic Field Laboratory facilities is from the NSF: NSF-DMR-2128556. Work done by M. Barron at Jefferson lab was supported by the U S National Science Foundation Research Experience for Undergraduates at Old Dominion University Grant No. 1950141. This is authored by Jefferson Science Associates, LLC under U S DOE Contract No. DE-AC05-06OR23177.

ORCID iDs

B D Khanal https://orcid.org/0000-0001-9299-3123
S Balachandran https://orcid.org/0000-0002-0077-8504
S Chetri https://orcid.org/0000-0003-0633-379X
P J Lee https://orcid.org/0000-0002-8849-8995
G Ciovati https://orcid.org/0000-0001-9316-7704
P Dhakal https://orcid.org/0000-0002-9381-4091

References

[1] Padamsee H 2017 50 years of success for srf accelerators–a review *Supercond. Sci. Technol.* **30** 053003
[2] Krasnok A, Dhakal P, Fedorov A, Frigola P, Kelly M and Kutsaev S 2024 Superconducting microwave cavities and qubits for quantum information systems *Appl. Phys. Rev.* **11** 011302
[3] Dhakal P *et al* 2013 Effect of high temperature heat treatments on the quality factor of a large-grain superconducting radio-frequency niobium cavity *Phys. Rev. Spec. Top. Accel.* **16** 042001
[4] Grassellino A, Romanenko A, Sergatskov D, Melnychuk O, Trenikhina Y, Crawford A, Rowe A, Wong M, Khabiboulline T and Barkov F 2013 Nitrogen and argon doping of niobium for superconducting radio frequency cavities: a pathway to highly efficient accelerating structures *Supercond. Sci. Technol.* **26** 102001
[5] Dhakal P, Ciovati G, Kneisel P and Myneni G R 2014 Enhancement in quality factor of SRF niobium cavities by material diffusion *IEEE Trans. Appl. Supercond.* **25** 1
[6] Dhakal P 2020 Nitrogen doping and infusion in SRF cavities: a review *Phys. Open* **5** 100034
[7] Posen S, Romanenko A, Grassellino A, Melnychuk O and Sergatskov D 2020 Ultralow surface resistance via vacuum heat treatment of superconducting radio-frequency cavities *Phys. Rev. Appl.* **13** 014024
[8] Ito H, Araki H, Takahashi K and Umemori K 2021 Influence of furnace baking on Q–E behavior of superconducting accelerating cavities *Prog. Theor. Exp.* **2021** 071G01
[9] Lechner E, Angle J, Stevie F, Kelley M, Reece C and Palczewski A 2021 RF surface resistance tuning of superconducting niobium via thermal diffusion of native oxide *Appl. Phys. Lett.* **119** 082601
[10] Dhakal P, Khanal B D, Gurevich A and Ciovati G 2024 Field, frequency and temperature dependencies of the surface resistance of nitrogen diffused niobium superconducting radio frequency cavities *Phys. Rev. Accel. Beams* **27** 062001
[11] Gonnella D *et al* 2015 Nitrogen-doped 9-cell cavity performance in a test cryomodule for LCLS-II *J. Appl. Phys.* **117** 023908
[12] Kneisel P, Ciovati G, Dhakal P, Saito K, Singer W, Singer X and Myneni G 2015 Review of ingot niobium as a material for superconducting radiofrequency accelerating cavities *Nucl. Instrum. Methods Phys. Res.* A **774** 133
[13] Myneni G *et al* 2023 Medium grain niobium SRF cavity production technology for science frontiers and accelerator applications *J. Instrum.* **18** T04005
[14] Vogt J-M, Kugeler O and Knobloch J 2013 Impact of cooldown conditions at T_c on the superconducting RF cavity quality factor *Phys. Rev. Spec. Top.-Accel. Beams* **16** 102002
[15] Romanenko A, Grassellino A, Melnychuk O and Sergatskov D 2014 Dependence of the residual surface resistance of superconducting radio frequency cavities on the cooling dynamics around T_c *J. Appl. Phys.* **115** 184903
[16] Gonnella D, Kaufman J and Liepe M 2016 Impact of nitrogen doping of niobium superconducting cavities on the sensitivity of surface resistance to trapped magnetic flux *J. Appl. Phys.* **119** 073904
[17] Martinello M, Checchin M, Grassellino A, Crawford A, Melnychuk O, Romanenko A and Sergatskov D 2015 Magnetic flux studies in horizontally cooled elliptical superconducting cavities *J. Appl. Phys.* **118** 044505
[18] Vogt J-M, Kugeler O and Knobloch J 2015 High-q operation of superconducting rf cavities: potential impact of thermocurrents on the RF surface resistance *Phys. Rev. Spec. Top.-Accel. Beams* **18** 042001
[19] Kubo T 2016 Flux trapping in superconducting accelerating cavities during cooling down with a spatial temperature gradient *Prog. Theor. Exp. Phys.* **2016** 053G01
[20] Posen S *et al* 2019 Role of magnetic flux expulsion to reach $Q_0 > 3\times10^{10}$ in superconducting RF cryomodules *Phys. Rev. Accel. Beams* **22** 032001
[21] Sung Z H, Kulyavtsev P, Martinello M, Gonnella D, Ross M and Posen S 2023 Evaluation of predictive correlation between flux expulsion and grain growth for superconducting radio frequency cavities *Supercond. Sci. Technol.* **36** 095015
[22] Balachandran S, Polyanskii A, Chetri S, Dhakal P, Su Y-F, Sung Z-H and Lee P J 2021 Direct evidence of microstructure dependence of magnetic flux trapping in niobium *Sci. Rep.* **11** 1
[23] Antoine C 2012 Materials and surface aspects in the development of SRF Niobium cavities *type Tech. Rep.* EuCARD-BOO-2012-001 (available at: https://cds.cern.ch/record/1472363)
[24] Antoine C Z 2019 Influence of crystalline structure on RF dissipation in superconducting niobium *Phys. Rev. Accel. Beams* **22** 034801
[25] Wang M, Polyanskii A, Balachandran S, Chetri S, Crimp M A, Lee P J and Bieler T R 2022 Investigation of the effect of structural defects from hydride precipitation on superconducting properties of high purity SRF cavity Nb using magneto-optical and electron imaging methods *Supercond. Sci. Technol.* **35** 045001
[26] Dhakal P, Ciovati G and Gurevich A 2020 Flux expulsion in niobium superconducting radio-frequency cavities of different purity and essential contributions to the flux sensitivity *Phys. Rev. Accel. Beams* **23** 023102

[27] Martinello M, Grassellino A, Checchin M, Romanenko A, Melnychuk O, Sergatskov D, Posen S and Zasadzinski J F 2016 Effect of interstitial impurities on the field dependent microwave surface resistance of niobium *Appl. Phys. Lett.* **109** 062601

[28] Checchin M, Martinello M, Grassellino A, Aderhold S, Chandrasekaran S K, Melnychuk O, Posen S, Romanenko A and Sergatskov D A 2018 Frequency dependence of trapped flux sensitivity in SRF cavities *Appl. Phys. Lett.* **112** 072601

[29] Ciovati G, Dhakal P, Matalevich J, Myneni G, Schmidt A, Iversen J, Matheisen A and Singer W 2015 Mechanical properties of niobium radio-frequency cavities *Mater. Sci. Eng.* A **642** 117

[30] Gonnella D *et al* 2018 Industrialization of the nitrogen-doping preparation for SRF cavities for LCLS-II *Nucl. Instrum. Methods Phys. Res.* A **883** 143

[31] Khanal B, Balachandran S, Chetri S, Dhakal P and Lee P 2022 Magnetic flux expulsion in superconducting radio-frequency niobium cavities made from cold worked niobium *Proc. NAPAC'22, Series and Number SeriesInternational Particle Accelerator Conf. No.number5* (JACoW Publishing) pp 611–4

[32] Umezawa H 2003 Impurities analysis of high purity niobium in industrial production *Mater. Tech.* **91** 33–37

[33] Aune B *et al* 2000 Superconducting tesla cavities *Spec.Top.-Accel. Beams* **3** 092001

[34] Brandt E H 2000 Superconductors in realistic geometries: geometric edge barrier versus *pinning Physica C* **332** 99

[35] Ciovati G, Dhakal P, Parajuli I, Saeki T and Pathiranage M W 2022 Thermal conductivity of electroplated copper onto bulk niobium at cryogenic temperatures *Proc. SRF'21*, Series and Number SeriesInternational Conf. on RF Superconductivity No. Number20 (JACoW Publishing) pp 576–80

[36] ASTM Standard test method for microindentation hardness of materials (available at: www.astm.org/e0384-05.html)

[37] Mattis D C and Bardeen J 1958 Theory of the anomalous skin effect in normal and superconducting metals *Phys. Rev.* **111** 412

[38] Halbritter J 1970 Fortan program for the comutation of the surface impedance of superconductors *type Tech. Rep.* (Institution Kernforschungszentrum)

[39] Gurevich A 2017 Theory of RF superconductivity for resonant cavities *Supercond. Sci. Technol.* **30** 034004

[40] Gorter C J and Casimir H 1935 Zur Thermodynamik des Supraleitenden Zustandes *Archives du Musée Teyler* (Springer) pp 55–60

[41] Pippard A B and Bragg W L 1953 An experimental and theoretical study of the relation between magnetic field and current in a superconductor *Proc. R. Soc.* A **216** 547

[42] Humphreys F J and Hatherly M 2012 *Recrystallization and Related Annealing Phenomena* (Elsevier)

[43] Xu P 2019 *Investigation of the Thermal Transport in Superconducting Niobium and Tantalum* (Michigan State University)

[44] Balachandran S, Xu P, Dhakal P, Carl M, Walsh R and Lee P 2023 Effect of strain on the resistivity and thermal conductivity of high purity niobium *IEEE Trans. Appl. Supercond.* **33** 1

[45] Dhavale A S, Dhakal P, Polyanskii A A and Ciovati G 2012 Flux pinning characteristics in cylindrical niobium samples used for superconducting radio frequency cavity fabrication *Supercond. Sci. Technol.* **25** 065014

[46] Dew-Hughes D 1974 Flux pinning mechanisms in type ii superconductors *Phil. Mag.* **30** 293

[47] Cordero Z C, Knight B E and Schuh C A 2016 Six decades of the hall–petch effect–a survey of grain-size strengthening studies on pure metals *Int. Mater. Rev.* **61** 495

[48] Umezawa M Y H and Nishida N 2024 Relationship between anisotropy and cross rolling process for high purity niobium sheets *Proc. IPAC'24, Series and Number 15* (JACoW Publishing) pp 3893–6

[49] Yamanaka M and Shimada K 2023 Relation between tensile strength and annealing temperature for high purity niobium *IEEE Trans. Appl. Supercond.* **33** 1

[50] Sakharov N and Chuvil'deev V 2022 Analysis of the effect of impurities on primary recrystallization in pure metals *Phys. Met. Metallogr.* **123** 797

[51] Thune Z, McKinney C, Fleming N and Bieler T 2023 The influence of strain path and heat treatment variations on recrystallization in cold-rolled high-purity niobium polycrystals *IEEE Trans. Appl. Supercond.* **33** 1

[52] Thune Z and Bieler T 2023 The influence of sample preparation, soak time and heating rate on measured recrystallization of deformed polycrystalline niobium *Proc. SRF'23*

[53] Balachandran S, Bieler T, Chetri S, Dhakal P, Lee P, Thune Z and Valente-Feliciano A-M 2023 Microstructure development in a cold worked srf niobium sheet after heat treatments *Proc. SRF'23, Series and Number SeriesInternational Conf. on RF Superconductivity No. Number21* (JACoW Publishing) pp 191–6

[54] Martinello M, Sung Z-H, Posen S, Lee J, Grassellino A and Romanenko A 2019 Microscopic investigation of flux trapping sites in bulk NB *19th Int. Conf. on RF Superconductivity (SRF'19) (Dresden, Germany)*

[55] Sun Z, Baraissov Z, Dukes C A, Dare D K, Oseroff T, Thompson M O, Muller D A and Liepe M U 2023 Surface oxides, carbides and impurities on RF superconducting nb and nb$_3$sn: a comprehensive analysis *Supercond. Sci. Technol.* **36** 115030

[56] Dangwal Pandey A *et al* 2021 Grain boundary segregation and carbide precipitation in heat treated niobium superconducting radio frequency cavities *Appl. Phys. Lett.* **119** 194102

[57] Chen Z *et al* 2024 Unraveling the nanoscale segregation mechanism in n-doped niobium for enhanced SRF performance *Small Methods* **8** 2301319

[58] Semione G D L *et al* 2019 Niobium near-surface composition during nitrogen infusion relevant for superconducting radio-frequency cavities *Phys. Rev. Accel. Beams* **22** 103102

[59] Peterson T, Carter H, Foley M, Klebaner A, Nicol T, Page T, Theilacker J, Wands R, Wong-Squires M and Wu G 2010 Pure niobium as a pressure vessel material *AIP Conf. Proc.* **1218** 839–48

[60] Myneni G R and Agnew S 2003 Elasto-plastic behavior of high RRR niobium: effects of crystallographic texture, microstructure and hydrogen concentration *AIP Conf. Proc.* **671** 227–42

[61] Dhakal P, Ciovati G, Pudasaini U, Chetri S, Balachandran S and Lee P J 2019 Surface characterization of nitrogen-doped high purity niobium coupons compared with superconducting RF cavity performance *Phys. Rev. Accel. Beams* **22** 122002

[62] Lechner E M, Angle J W, Baxley C, Kelley M J and Reece C E 2023 Topographic evolution of heat-treated NB upon electropolishing for superconducting RF applications *Phys. Rev. Accel. Beams* **26** 103101

[63] Kim M, Chen K, Carriere P, Matavalam N, Penney J, Kutsaev S and Korkolis Y P 2022 Mechanical behavior and forming of commercially-pure niobium sheet *Int. J. Solids Struct.* **257** 111770

[64] Hecker S S 1975 Simple technique for determining forming limit curves *Sheet Met. Ind.* **52** 671

[65] Khanal B and Dhakal P 2023 Evaluation of flux expulsion and flux trapping sensitivity of SRF cavities fabricated from cold work Nb sheet with successive heat treatment *Proc. SRF'23* (JACoW Publishing)